

Tidal fluctuations and spatial heterogeneity lead to trapping and chaotic mixing in coastal aquifers

Satoshi Tajima¹, Marco Dentz²

¹Graduate School of Frontier Sciences, The University of Tokyo, Tokyo, Japan
²Spanish National Research Council (IDAEA-CSIC), Barcelona, Spain

arXiv:2503.02516v1 [physics.flu-dyn] 4 Mar 2025

Corresponding author: Satoshi Tajima, m@st-gw.net

Abstract

The combined effect of tidal forcing and aquifer heterogeneity leads to intricate transport patterns in coastal aquifers that impact both on solute residence times and mixing dynamics. We study these patterns through detailed numerical simulations of density-dependent flow and transport in a three-dimensional heterogeneous coastal aquifer under tidal forcing. Advective particle tracking from both the freshwater and seawater domains reveals the formation of chaotic and periodic orbits in the freshwater-saltwater transition zone that may persistently trap contaminants. We find that increasing heterogeneity results in increased trapping, but also increased mixing entropy, which suggests that the chaotic orbits enhance mixing between contaminants from the freshwater and seawater domains. These findings highlight on the one hand, the long-term contamination risks of coastal aquifers through trapping, and on the other hand, the creation of hotspots for chemical and biological reactions through chaotic mixing in the transition zone.

1 Introduction

Coastal aquifers are characterised by dynamic interactions between seawater and freshwater, where the interplay between tidal fluctuations, spatial heterogeneity and aquifer compressibility play a significant role (Werner et al., 2013). These processes collectively govern flow dynamics, salinity distribution, and contaminant transport within coastal aquifers. Density effects between seawater and freshwater lead to the formation of a saltwater wedge that intrudes into the coastal aquifer. Within the wedge, seawater recirculates from the seaward boundary, while freshwater flows over the seawater body from the land (Werner et al., 2013). At the interface between saltwater and freshwater, a mixing or transition zone is created that represents a hotspot for chemical and biological activity (Sanford & Konikow, 1989; Moore, 1999a; Rezaei et al., 2005; Spiteri et al., 2008; De Vriendt et al., 2020). These processes are subject to spatial heterogeneity in the hydraulic aquifer properties and tidal fluctuations, which impact the groundwater flow patterns, the dispersion of the transition zone, the mixing between salt and freshwater, and the mixing and dispersion of contaminants in the aquifer.

Studies in homogeneous and layered coastal aquifers have shown that tidal fluctuations expand the transition zone between salt and freshwater (Oberdorfer et al., 1990; Inouchi et al., 1990; Pool et al., 2014). Furthermore, Pool et al. (2015) showed that spatial aquifer heterogeneity mitigates the impact of tidal fluctuations on the width of the mixing zone between salt and freshwater, whereas increased aquifer compressibility leads to an amplification. Using lithology of coastal aquifers, Michael et al. (2016) found that heterogeneity creates complex spatial salinity distributions that lead to groundwater circulation rates that cannot be captured by models based on equivalent homogeneous media. For intertidal aquifers, Geng, Michael, et al. (2020) found that spatial heterogeneity creates topological flow characteristics that encompass spatiotemporal patterns and regions of intense and low mixing. Regions of strong mixing are amplified by spatial heterogeneity, which leads to the emergence of reaction hotspots along the saltwater-freshwater interface (Pool & Dentz, 2018), and facilitates the propagation of karst in coastal aquifers (De Vriendt et al., 2020).

The flow patterns in coastal aquifers induced by tidal fluctuations, buoyancy and spatial heterogeneity also determine the transport, mixing and reaction behaviour of sea and land borne contaminants (C. E. Robinson et al., 2018; Santos et al., 2021). Geng, Boufadel, et al. (2020) analysed solute transport in heterogeneous beach aquifers subject to tidal sea level fluctuations. They found that spatial heterogeneity enhances the spreading of a contaminant plume and the generation of transient preferential flow paths and highly variable solute transit times, and related these behaviours to the flow topology. For constant density flows, the interplay between temporal flow fluctuations, spatial heterogeneity and aquifer compressibility can generate Lagrangian coherent struc-

tures and induce chaotic advection and mixing (Trefry et al., 2019, 2020; Wu et al., 2024; Tajima & Dentz, 2024). Trefry et al. (2019) investigated advective transport in horizontal two-dimensional heterogeneous confined aquifers under temporal forcing superposed to a regional flow gradient. They find that heterogeneity and periodic temporal forcing generates chaotic advection and Lagrangian coherent structures near the forced boundary, which enhances fluid mixing and transport and leads to anomalous residence time distributions, see also Wu et al. (2020). Tajima and Dentz (2024) analysed the spreading of displacement fronts in two-dimensional heterogeneous aquifers driven by transient forcing. They observe the creation of stable and chaotic regions, which leads to containment and at the same time may promote mixing.

In this paper, we investigate the combined effect of buoyancy, tidal forcing and aquifer heterogeneity on flow and transport patterns in three-dimensional, heterogeneous coastal aquifers. To this end, we analyze particle paths originating from the sea and land boundaries to analyze the chaotic flow behaviour in terms of Poincaré sections. The analysis of residence time distributions in the aquifer elucidates further the creation of periodic and chaotic orbits, quantifying how contaminants can be trapped in the transition zone between seawater and freshwater. The evolution of the mixing entropy and segregation intensity demonstrates how spatial heterogeneity leads to the mixing of sea and land borne solutes.

2 Methods

We consider density-dependent flow in a fully saturated, three-dimensional, heterogeneous coastal aquifer under tidal forcing. The setup and dimensions of the model domain are illustrated in Figure 1. In the following, we outline the generation of the spatially variable hydraulic conductivity field, the governing equations for variable-density flow and particle tracking and their numerical solution, as well as the observables that are used to elucidate the Lagrangian flow kinematics, and the mixing potential.

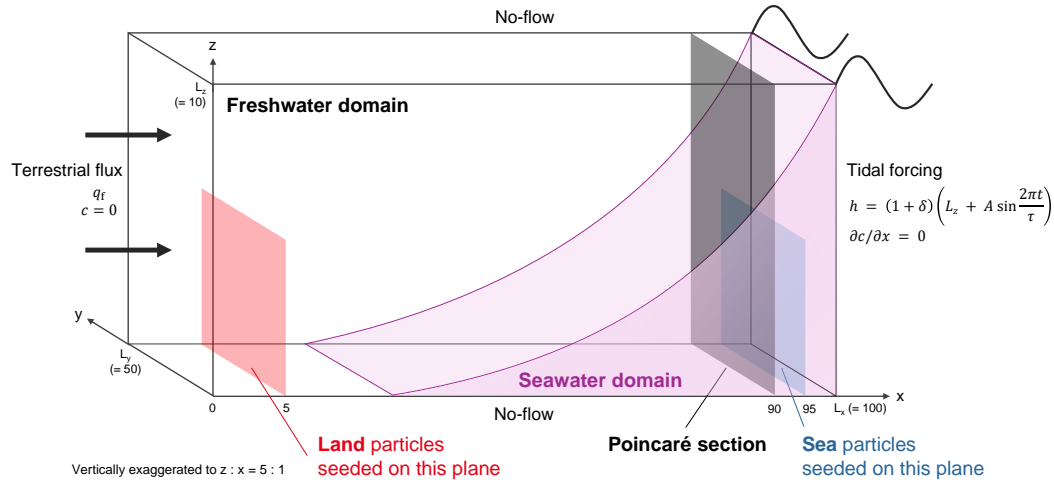


Figure 1. Schematic of model domain. Salinity distribution shown here is conceptual and not simulated result.

2.1 Hydraulic conductivity

To systematically represent spatial aquifer heterogeneity, the hydraulic conductivity, which is assumed scalar for simplicity, is modelled as a multi-Gaussian random space function (Rubin, 2003). We consider the hydraulic conductivity $K_0(\mathbf{x})$, which is referred to the freshwater density, that is, $K_0(\mathbf{x}) = k_0(\mathbf{x})/\rho_0 g$, where ρ_0 is the freshwater density, g is gravitational acceleration and $k(\mathbf{x})$ is permeability. Here, the log-hydraulic conductivity $f(\mathbf{x}) = \ln K_0(\mathbf{x})$ is modelled as a correlated Gaussian random space function. It has a constant mean $\overline{f(\mathbf{x})} = \ln K_G$, where K_G is the geometric mean conductivity which is at the same time the effective conductivity (Renard & De Marsily, 1997). Furthermore, we employ the exponential covariance function

$$C_f(\mathbf{x}) = \sigma_f^2 \exp \left[-\sqrt{(x^2 + y^2)/\lambda_{\parallel}^2 + z^2/\lambda_{\perp}^2} \right] \quad (1)$$

where σ_f^2 is the variance of $f(\mathbf{x})$, $\lambda_{\parallel} = 5$ m is the correlation length in the x - y plane, and $\lambda_{\perp} = 2$ m is the correlation length in the transverse direction. To quantify the effect of heterogeneity on the transport and mixing behaviour, we consider $\sigma_f^2 = 0.5, 1, 2, 4$. For each case, 20 realizations of the hydraulic conductivity are generated. A complete list of the modelling parameters is given in Appendix.

2.2 Variable-density groundwater flow

The variable density groundwater flow model follows the formulation of Langevin et al. (2020). Specifically, we use the Oberbeck-Boussinesq approximation, which disregards density variations in the continuity equation. With this approximation, the continuity equation is given by

$$S_s \frac{\partial h(\mathbf{x}, t)}{\partial t} + \nabla \cdot \mathbf{q}(\mathbf{x}, t) = 0, \quad (2)$$

where S_s is the specific storativity, $h(\mathbf{x}, t)$ is the hydraulic head, and $\mathbf{q}(\mathbf{x}, t)$ is the specific discharge. Momentum conservation is described by the Darcy equation in hydraulic head form (Langevin et al., 2020)

$$\mathbf{q}(\mathbf{x}, t) = -K_0(\mathbf{x}) \left\{ \frac{\rho(c)}{\rho_0} \nabla h(\mathbf{x}, t) + [h(\mathbf{x}, t) - z] \frac{\nabla \rho(c)}{\rho_0} \right\}. \quad (3)$$

The fluid density $\rho(c)$ is assumed to depend linearly on the salt concentration $c(\mathbf{x}, t)$, that is, $\rho(c) = \rho_0[1 + \epsilon c(\mathbf{x}, t)/c_s]$, where c_s is the constant salt concentration in seawater, and ρ_0 is the reference density of freshwater. The evolution of the salt concentration $c(\mathbf{x}, t)$ is described by the advection-dispersion equation

$$\frac{\partial c(\mathbf{x}, t)}{\partial t} + \nabla \cdot [\mathbf{u}(\mathbf{x}, t)c(\mathbf{x}, t)] - \nabla \cdot [\mathbf{D}(\mathbf{x}, t)\nabla c(\mathbf{x}, t)] = 0, \quad (4)$$

where $\mathbf{u}(\mathbf{x}, t) = \mathbf{q}(\mathbf{x}, t)/\phi$ is the porewater velocity, and ϕ is the porosity. The local hydrodynamic dispersion tensor $\mathbf{D}(\mathbf{x}, t)$ is given by (Bear, 1972)

$$D_{ij}(\mathbf{x}, t) = D_m \delta_{ij} + \delta_{ij} \alpha_I |\mathbf{u}(\mathbf{x}, t)| + (\alpha_I - \alpha_{II}) \frac{u_i(\mathbf{x}, t)u_j(\mathbf{x}, t)}{|\mathbf{u}(\mathbf{x}, t)|}, \quad (5)$$

where D_m is the molecular diffusion, α_I and α_{II} are the longitudinal and transverse dispersivity, respectively. Terrestrial freshwater flux q_f with zero salinity ($c = 0$) is applied to the inland lateral boundary ($x = 0$). The sea boundary ($x = L_x$) is forced with tides, expressed by sinusoidal fluctuations in hydraulic head as

$$h(\mathbf{x}, t)|_{x=L_x} = L_z + A \sin \frac{2\pi t}{\tau}, \quad (6)$$

where t is the time, A is the amplitude, and τ is the period. Here, we assume a semidiurnal ($\tau = 0.5$ d) tide with an amplitude of $A = 0.5$ m (Schwidorski, 1980; Pool et

al., 2014, 2015; Schrama & Ray, 1994). Using these values for tidal properties and a specific discharge of $S_s = 1 \times 10^{-2} \text{ m}^{-1}$, the tidal mixing number (Pool et al., 2014) is $n_{\text{tm}} \equiv \sqrt{\tau K_G / S_s} / A \approx 26.5 \leq 600$, indicating the potential for significant tidal effects on mixing and spreading (Pool et al., 2015). These boundary conditions create mean flow from the inland boundary at $x = 0$ towards the coastal boundary at $x = L_x$, aligned with the x - and z - axes and perpendicular to the y -axis. The coastal boundary is assumed to be a no-dispersion boundary ($\partial c / \partial x = 0$). This means that, if inflow from the sea to the model domain occurs, the concentration at the boundary is identical to the normalised salinity of seawater ($c = 1$) (e.g. Pool et al., 2014; Tajima et al., 2022; Tajima, Liu, & Tokunaga, 2024). In contrast, if outflow from the domain occurs, the boundary concentration becomes identical to that of the discharging groundwater. The other boundaries are assumed to be no-flow. The boundary conditions are summarised in Figure 1, and the modelling parameters are summarized in Appendix.

The numerical simulations based on the density-dependent flow and transport system given by equations (2)–(4) are performed with MODFLOW 6 (Langevin et al., 2017). The model domain is spatially discretised so that the mesh Péclet number is below 2 throughout the domain to ensure convergence. We first perform simulations without tidal fluctuations until a quasi-steady state. Tidal fluctuations are then included, and the simulations are run until a dynamic steady state is reached, where the temporal fluctuations in the head and salinity distributions become stable.

2.3 Particle tracking

To explore the impact of tidal fluctuations, heterogeneity and variable density on solute transport, we analyze advective particle trajectories originating from the sea and land boundaries. We focus on the distribution of residence times in the system and the advective interpenetration of particle trajectories in the seawater- and freshwater-dominated aquifer regions. Advective particle tracking elucidates the Lagrangian kinematics and transport structure of the flow (Wu et al., 2020). The trajectory of a particle is given by the kinematic equation (Kubo et al., 2012),

$$\frac{d\mathbf{x}(t, \mathbf{a})}{dt} = \mathbf{u}[\mathbf{x}(t, \mathbf{a}), t], \quad (7)$$

where $\mathbf{x}(t, \mathbf{a})$ is the particle position at time t with origin at $\mathbf{x}(t = 0, \mathbf{a}) = \mathbf{a}$. We consider two families of particles with different initial positions at $t = 0$. Each family is vertically aligned on a single $y - z$ cross section within $2.5 \leq y \leq 47.5 \text{ m}$ and $1 \leq z \leq 5 \text{ m}$. The "sea" family (coloured in red) is located at a plane at $x = 5 \text{ m}$, whereas the "land" family (coloured in blue) at $x = 95 \text{ m}$ as illustrated in Figure 1. Equation 7 is numerically solved using a third-order Runge-Kutta method (Tajima, Dentz, et al., 2024; Tajima & Dentz, 2024). Further details on the setup of the numerical particle tracking simulations are given in Appendix.

2.4 Observables

From the simulated particle trajectories, we investigate the Lagrangian kinematics and residence time distributions of the flows. The evaluation of residence times gives insight in whether there are closed orbits in which particles can get trapped. To analyze the types of flows that may occur, we also determine Poincaré sections. To assess the mixing of particles originating from the sea and land boundaries, we consider the mixing entropy and segregation index as outlined below.

2.4.1 Residence time distributions

The residence time distributions from the land and sea boundaries are denoted by $R_L(t)$ and $R_S(t)$, respectively. We consider the cumulative distributions $R_i(t) \equiv n_i(t) / n_{0,i}$

($i = L, S$), where $n_i(t)$ is the number of particles from the land ($i = L$) and sea ($i = S$) boundaries that have discharged over the sea boundary before time t , and $n_{0,i}$ the respective total number of particles. Thus, $R_i(t)$ is equal to the fraction of particles that have discharged from the domain by time t relative to the initial number of particles, or, equivalently, the probability that the residence time is smaller than t . These observables are determined from the respective advective travel times to the sea boundary. That is, for $R_L(t)$, the travel time from the land to the sea boundary, and for $R_S(t)$, the travel time from the sea to the sea boundary. The trapping of particles along periodic or aperiodic orbits leads to infinite residence times, which manifests in asymptotic values of $R_i(t)$ smaller than 1.

2.4.2 Poincaré sections

To analyze the Lagrangian kinematics and transport structure of the flow driven by the interplay of tidal forcing and aquifer heterogeneity, we investigate Poincaré sections. While three-dimensional particle trajectories may be complex and are in general more diffusive to visualize, Poincaré sections represent the distribution of intersection points of advective particle trajectories on a two-dimensional plane, oriented perpendicular to the mean flow and aligned with the y - and z - axes as illustrated in Figure 1. The Poincaré section represents a mapping of the plane onto itself. The times between intersections are generally not constant (Strogatz, 2001). Periodic orbits intersect the plane always at the same point, quasi-periodic orbits at a finite set of points or along a closed curve in the plane. Non-periodic orbits intersect the plane at each iteration at a different point, which indicates chaotic mixing. Here we consider two families of particles according to their origin at the sea and land boundaries marked by blue and red, respectively. For tidally-forced variable density flow in a homogeneous aquifer, there are no recurring trajectories, that is, each trajectory intersects the target plane only once. Therefore, the number of intersections remains constant in time. As we will see in the following, this is different for heterogeneous aquifers; we will observe both periodic and aperiodic orbits, which are commensurate with the trapping of particles. Non-periodic orbits lead to an increase of the number of intersection points in the plane with the number of iterations. Note that the Poincaré sections considered here are different from the ones considered in Wu et al. (2024) and Tajima and Dentz (2024) for two-dimensional constant density flow in periodically forced aquifers. These authors define Poincaré section as a stroboscopic map capturing the locations of advected particles at each flow period. In other words, the Poincaré sections in these works generate a lower-dimensional subspace in a temporal domain by sampling particle positions at discrete time intervals corresponding to tidal periods. In contrast, the Poincaré sections considered in this work record intersection points on a two-dimensional plane from three-dimensional particle trajectories.

2.4.3 Mixing entropy

In order to assess the potential of the two families of particles to mix, we use the concept of mixing entropy. Specifically, to determine the degree of mixing between the two families and among each family separately, we apply the Shannon entropy measure proposed by Camesasca et al. (2006) to the set of points or dots of different colour on the Poincaré sections at $x = 90$ m. To do so, we discretize the plane into a square grid of grid length Δx . Then, we define the joint probability $p_{j,k}$ that a point on the Poincaré section belongs to family j ($j = S$ denotes the blue particles from the sea boundary, and $j = L$ the red particles from the land) and resides in bin k ,

$$p_{j,k} = \frac{n_{j,k}}{\sum_{j,k} n_{j,k}}, \quad (8)$$

where $n_{j,k}$ is the cumulative number of intersection points of the family j in bin k . The joint distribution $p_{j,k}$ can be expanded using the Bayes formula as $p_{j,k} = p_{j|k}p_k$, where

$$p_{j|k} = \frac{n_{j,k}}{\sum_j n_{j,k}}, \quad p_k = \frac{n_k}{\sum_k n_k}, \quad n_k = \sum_j n_{j,k}. \quad (9)$$

That is, $p_{j|k}$ is the probability that an intersection point that is in bin k belongs to family j , and p_k is the probability of finding an intersection point in bin k . The entropy H of the distribution of intersection points is then defined by

$$H = - \sum_{j,k} p_{j,k} \ln(p_{j,k}). \quad (10)$$

Using the decomposition $p_{j,k} = p_{j|k}p_k$, it can be written as $H = H_c + H_s$, where H_c denotes the mixing entropy between the two families, or colours, and H_s of the distribution of intersection points irrespective of the colour,

$$H_c = - \sum_k \left[p_k \sum_j p_{j|k} \ln(p_{j|k}) \right], \quad H_s = - \sum_k p_k \ln(p_k). \quad (11)$$

2.4.4 Segregation intensity

The segregation intensity of [Danckwerts \(1952\)](#) measures, as the name implies, the degree of segregation of the two colours (families). It is complementary to the mixing entropy defined in the previous section. We consider the same setup as in the previous section and want to determine the degree of segregation of the intersection points of different colours in the Poincaré section. Thus, the segregation intensity I is defined as

$$I = \frac{\sigma_r \sigma_b}{\bar{p}_r \bar{p}_b}. \quad (12)$$

The average probability \bar{p}_j of group j in the Poincaré section is

$$\bar{p}_j = \frac{1}{N} \sum_{k \in E} p_{j|k}, \quad (13)$$

with N is the total number of bins and $E = \{k | p_k \neq 0\}$. The standard deviation σ_j of the distribution of j is defined by

$$\sigma_j^2 = \frac{1}{N} \sum_{k \in E} (p_{j|k} - \bar{p}_j)^2. \quad (14)$$

For illustration, let us consider the situation of full segregation, as is the case for a homogeneous aquifer. The red dots of the land family are confined to a fraction ρ_r of the Poincaré section with constant density a_r and the blue dots of the sea family to the complement with fraction $\rho_b = 1 - \rho_r$ and constant density a_b . Then, the mean probability and variance are $\bar{p}_j = \rho_j a_j$ and $\sigma_j^2 = a_j^2 \rho_j (1 - \rho_j)$. In this case of full segregation, the segregation intensity is $I = 1$. In the case of full homogeneity, the distributions of red and blue dots are $p_j = \rho_j a_j$ with $j = r, b$. In this case, $\bar{p}_j = p_j$, $\sigma_j^2 = 0$, and the segregation intensity is $I = 0$.

3 Results and discussion

3.1 Emergence of confined pathlines and trapping

Figures 2a–c illustrate pathlines belonging to particles from the sea and land families for homogeneous and heterogeneous media up to time $t = 5 \times 10^4 \tau$ projected onto the $x-z$ plane. For the homogeneous medium, the pathlines do not intersect and are

fully segregated with the particles from the land boundary flowing over the seawater body and the seaward particles recirculating. This is different for heterogeneous media. In this case, we observe pathline crossing and twisting that can give rise to the emergence of periodic and chaotic orbits. For weakly heterogeneous media, the two families of pathlines remain mostly segregated, while they intersect within the families. In the recirculation zone, helical pathlines emerge, which manifest as closed lines on the $x - z$ projection. For increasing heterogeneity, pathlines from the two families cross each other and intertwine, that is, pathlines from the land boundary penetrate the recirculation zone, and cross pathlines from the sea boundary. The projections of pathlines in the recirculation zone describe closed orbits, which indicate helical flow. These orbits can lead to a significant increase in residence times or the trapping of solute particles.

Figures 2d and e show the cumulative distribution of residence times for particles originating from the land and sea boundaries. $R_L(t)$ and $R_S(t)$ increase over time, approaching a value of 1 as all the particles discharge across the sea boundary in the homogeneous case. With increasing heterogeneity, they evolve toward asymptotic values that are smaller than 1. For the homogeneous medium, the residence time distribution increases abruptly almost as a step function for $R_L(t)$, which indicates little dispersion along the pathlines. All the particles are recovered at a finite time. With increasing heterogeneity, the width of the residence time increases due to both early arrival due to preferential paths and very long arrival times due to trapping in recirculating paths. The numerical data indicate permanent trapping of up to 20% of the particles originating from the land and up to 35% of the particles originating from the sea boundary, which can be attributed to confined pathlines.

Figures 3a and b show Poincaré sections based on the pathlines of the particles whose residence times are above 3×10^4 s. The dots indicate the intersection points of the particle paths at a plane at $x = 90$ m from the sea boundary. We select a plane that intersects the recirculation zone close to the sea boundary illustrated in Figures 2 a-c. For the weakly heterogeneous medium with $\sigma_f^2 = 0.5$, the Poincaré section features a band of orbits of particles from the sea boundary. With increasing heterogeneity, for $\sigma_f^2 = 4$, red and blue dots are interspersed and dispersed across a larger area than for $\sigma_f^2 = 0.5$. This indicates the potential for mixing between water originating from the land and sea boundaries and contact between these waters for long times. It also indicates the emergence of chaotic orbits with increasing heterogeneity.

Chaotic and periodic orbits effectively trap particles within the domain, mixing particles and preventing their discharge into the sea. The retention of contaminants by the chaotic orbits in highly heterogeneous aquifers imply long-term contamination risks of coastal aquifers. These findings encompass not only contaminants but also nutrients from terrestrial sources that are discharged to the sea as submarine groundwater discharge (SGD) (Santos et al., 2021; Taniguchi et al., 2019). Such nutrient supply via SGD affects marine biota by supporting primary productivity (Waska & Kim, 2011, 2010; Blanco et al., 2011; Adolf et al., 2019), whereas excess nutrient loadings can lead to eutrophication (Hwang et al., 2005; Lee et al., 2009; Kwon et al., 2017; Cho et al., 2019). In light of these studies, our findings imply the reduced transport of nutrients from terrestrial sources to the sea via SGD, which might have multifaceted effects on marine ecosystems, potentially limiting primary productivity or alleviating eutrophication. Moreover, our results shed new light on the role of the recirculation region as a hotspot for intense chemical and biological reactions (Moore, 1999b; Heiss et al., 2017; C. Robinson et al., 2009; Liu et al., 2018).

3.2 Chaotic mixing between freshwater and seawater domains

To shed further light on the mixing of particles originating from land and sea boundaries, we analyze the distribution of intersection points on the Poincaré sections at $x =$

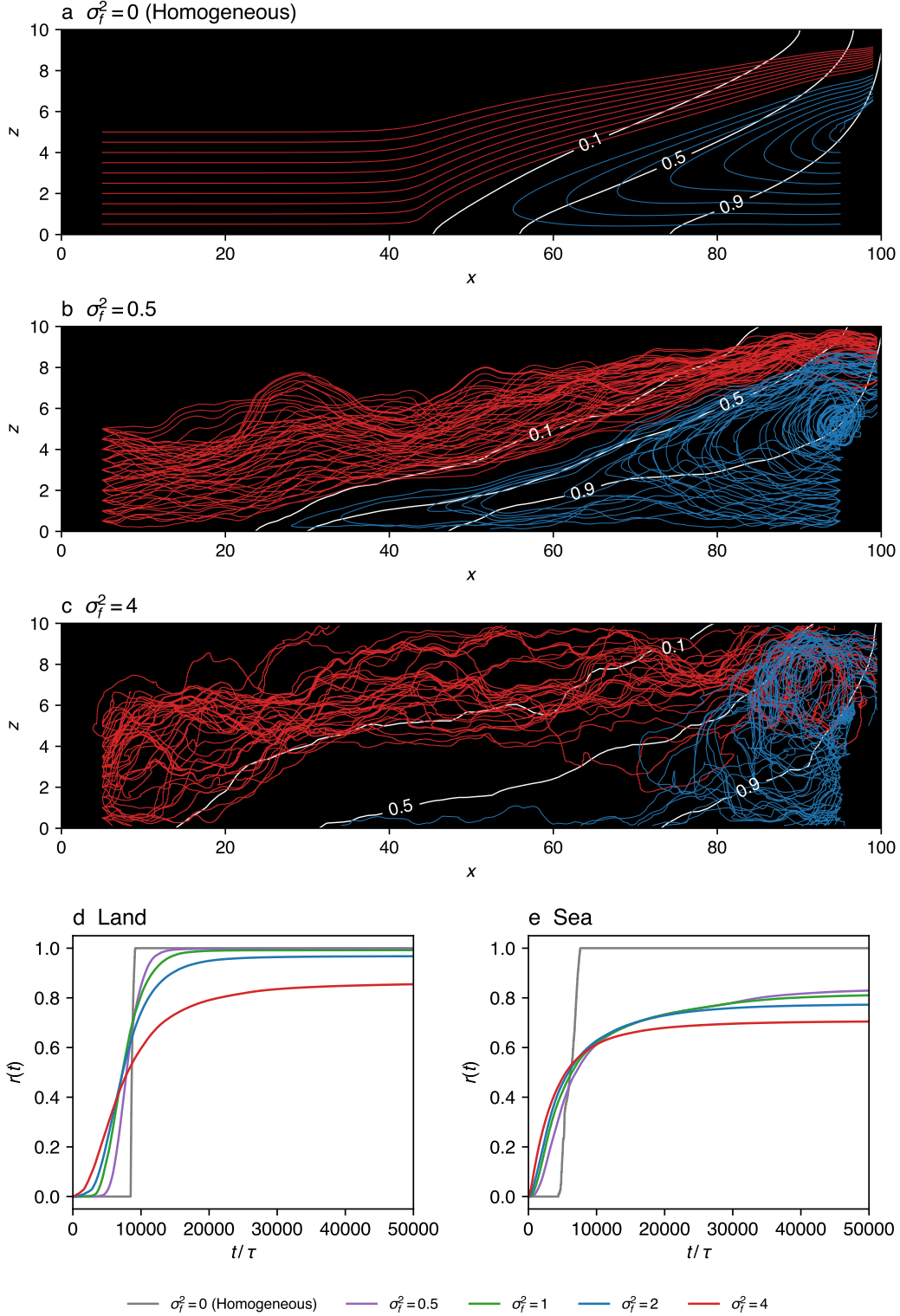


Figure 2. (a-c) Pathlines orthogonally projected onto $x - z$ plane, aligned with mean flow. Single realization is shown as example for each σ_f^2 . Red and blue colours correspond to land and sea families, respectively. White contours denote normalised salinity. (d, e) Cumulative breakthrough curves at the coastal boundary ($x = 0$) for particles originated from the (d) land ($x = 5$ m) and (e) sea boundaries ($x = 95$ m). Ensemble of 20 realizations for each σ_f^2 .

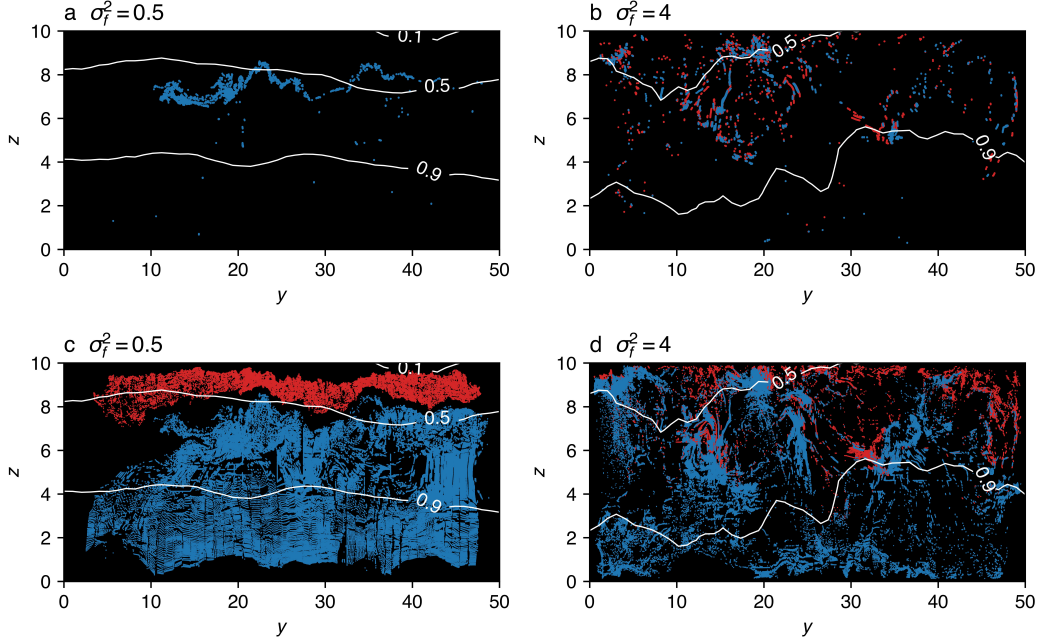


Figure 3. Poincaré sections at $x = 90$ m, perpendicular to mean flow, for $t/\tau \leq 5 \times 10^4$ for (a, b) particles with residence times above 3×10^4 s and (c, d) all particles. Single realization is shown as example for each σ_f^2 . Colour scheme is identical to that in Figures 2a–c.

90 m. Figures 3c and d show the intersection points of all particles from the land and sea boundaries. For weak heterogeneity ($\sigma_f^2 = 0.5$), the dots from the land (red) and sea (blue) families are well segregated, with the former confined to the freshwater domain and the latter to the seawater domain. For increasing heterogeneity ($\sigma_f^2 = 4$), in contrast, the two families intermix, with particles of the land family penetrating the seawater domain and vice versa. These findings indicate that the chaotic orbits, which emerge in the salinity transition zone near the coast, enhance the mixing between contaminants originating in the freshwater and seawater domains.

In order to quantify the quenching of dots belonging to the land and sea families, we determine the temporal evolution of the mixing entropy $H_c(t)$ and segregation intensity $I(t)$ between the two colours. Figures 4a and b show $H_c(t)$, which characterises the degree of mixing between the red and blue dots, and $I(t)$, which quantifies the degree of segregation between the two colours. $H_c(t)$ increases over time at a rate that increases with σ_f^2 towards an asymptotic value that describes the asymptotic mixing state between the two colours. Correspondingly, the segregation intensity $I(t)$ decreases over time at a rate that increases with increasing σ_f^2 , see Figure 4b. These observations show that the mixing between the land and sea families intensifies with increasing heterogeneity.

The existence and role of chaotic orbits for mixing is further corroborated by the cumulative number of intersection points in the Poincaré map. If all particles intersect only a finite number of times, the cumulative number converges to a constant value. Likewise, if pathlines describe periodic orbits, the number of intersections stabilizes at a constant value. This is what we observe in Figures 4c and d for particles originating from the land boundary for homogeneous and weakly heterogeneous media. For increasing heterogeneity, however, the number of intersections increases linearly with time both for the particles from the sea and land boundaries. This clearly indicates the existence of chaotic or quasi-periodic orbits that intersect the plane after each period at a different point.

Chaotic orbits are effective in enhancing mixing between contaminants originating from freshwater and seawater domains because the intersection points disperse across the Poincaré section.

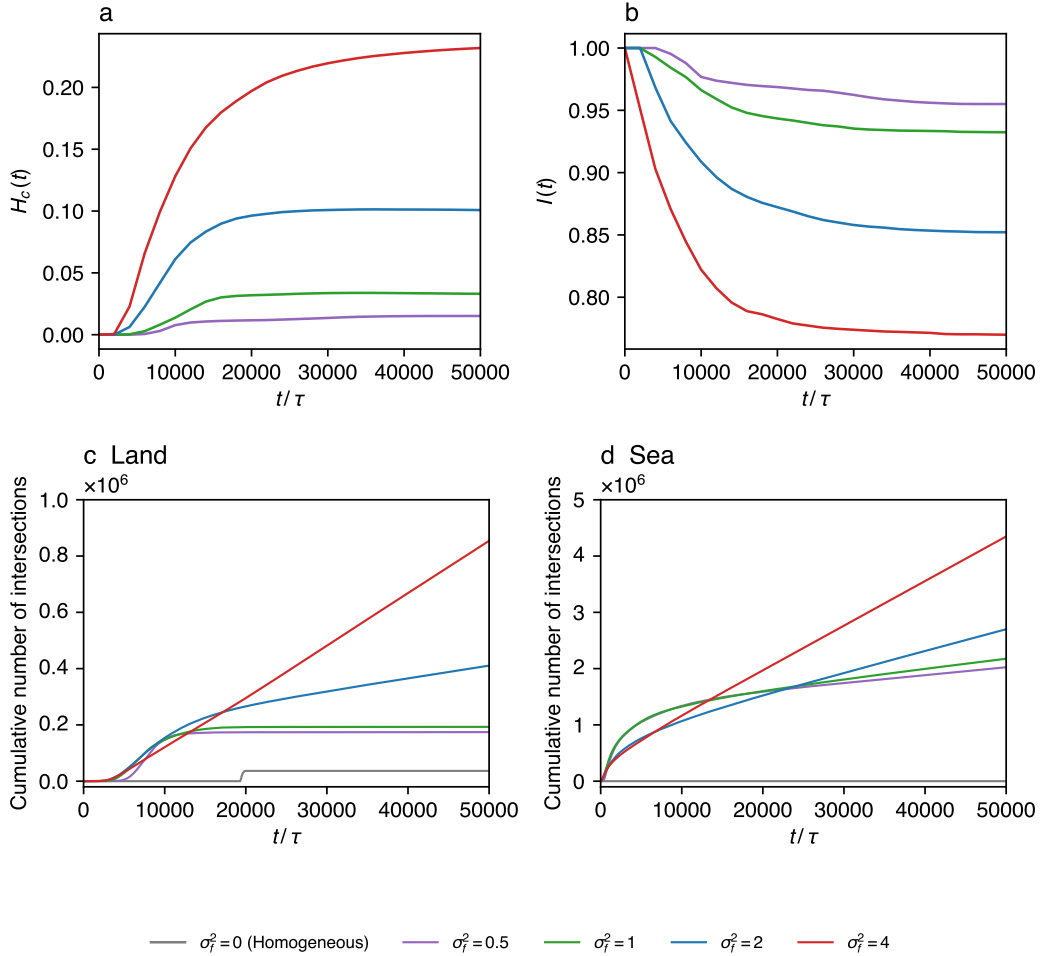


Figure 4. Temporal evolutions of (a) mixing entropy ($H_c(t)$), and (b) segregation intensity ($I(t)$), and (c, d) Cumulative number of intersection points for Poincaré sections in Figures 3c and d. Ensemble of 20 realisations for each σ_f^2 .

4 Conclusion

We investigate how the interplay of tidal forcing, buoyancy, and aquifer heterogeneity controls contaminant transport in coastal aquifers. Numerical simulations of variable density flow in three-dimensional heterogeneous aquifers provide evidence of the emergence of chaotic orbits and periodic orbits in the salinity transition zone near the coast with increasing heterogeneity. Closed orbits persistently trap contaminants within the aquifer, as seen in the distribution of solute residence times. The trapping of contaminants in closed orbits can pose long-term contamination risks in coastal aquifers with possible multifaceted impacts on marine ecosystems, potentially affecting nutrient-driven biological activity or eutrophication. On the other hand, chaotic orbits lead to enhanced mixing between salt and freshwater borne solute particles as evidenced by the behaviour

of the mixing entropy and segregation intensity. These results elucidate the mechanisms that convert the saltwater-freshwater transition zone into a hotspot for chemical and biological activity (e.g. Moore, 1999b; Heiss et al., 2017; C. Robinson et al., 2006, 2009). Furthermore, our findings suggest that chaotic behaviours in flow and transport processes can also occur during infrequent events, such as storm surges (e.g. Tajima et al., 2023), which are characterised by rapid changes in the flow field. These results underscore the critical importance of considering the interplay of tidal forcing, buoyancy and aquifer heterogeneity for the assessment of contaminant transport and chemical and biological activity in coastal aquifers.

Appendix A. Variable-density flow

We first note that fluid mass conservation is given by (Mulligan et al., 2011; Guo & Langevin, 2002)

$$\rho S_p \frac{\partial p(\mathbf{x}, t)}{\partial t} + \phi \frac{d\rho(c)}{dc} \frac{\partial c(\mathbf{x}, t)}{\partial t} + \nabla \cdot \rho \mathbf{q}(\mathbf{x}, t) = 0, \quad (1)$$

where S_p is specific storage in terms of pressure, $h(\mathbf{x}, t)$ hydraulic head, $\mathbf{q}(\mathbf{x}, t)$ specific discharge, ϕ porosity and $c(\mathbf{x}, t)$ is the volumetric salt concentration. The fluid density $\rho(c)$ is assumed to depend linearly on the salt concentration $c(\mathbf{x}, t)$, that is, $\rho(c) = \rho_0[1 + \epsilon c(\mathbf{x}, t)/c_s]$, where c_s is the constant salt concentration in seawater, and ρ_0 is the reference density of freshwater. Furthermore, we replace pressure by hydraulic head $p(\mathbf{x}, t) = h(\mathbf{x}, t)\rho g$, which gives

$$\rho S_f \frac{\partial h(\mathbf{x}, t)}{\partial t} + \rho S_f h(\mathbf{x}, t) \frac{d\rho(c)}{dc} \frac{\partial c(\mathbf{x}, t)}{\partial t} + \phi \frac{d\rho(c)}{dc} \frac{\partial c(\mathbf{x}, t)}{\partial t} + \nabla \cdot \rho \mathbf{q}(\mathbf{x}, t) = 0, \quad (2)$$

where we defined the specific storativity $S_f = \rho g S_p$. In the paper, we use the Oberbeck-Boussinesq approximation, which disregards density variations in the continuity equation. As pointed out by Guo and Langevin (2002), density effects in the continuity equation are important only for strong density contrasts. Thus, in the following we set (Langevin et al., 2020)

$$S_f \frac{\partial h(\mathbf{x}, t)}{\partial t} + \nabla \cdot \mathbf{q}(\mathbf{x}, t) = 0, \quad (3)$$

with $S_f = \rho_0 g S_p$.

Appendix B. Numerical scheme for particle tracking

For the readers' convenience, this supporting information summarises the numerical scheme for particle tracking simulations used in this study. The scheme follows the methods for purely advective transport in a two-dimensional domain in previous studies (Tajima, Dentz, et al., 2024; Tajima & Dentz, 2024), which is extended to three dimensions.

The Langevin equation is spatially discretised and numerically solved with the modified third-order Runge-Kutta method. The time step Δt is divided into three semi-time steps, and the particle location at the j th semi-time step is approximated by (Drummond et al., 1984; Tajima, Dentz, et al., 2024)

$$\mathbf{x}_j = \mathbf{x}_0 + \sum_{k=1}^j \alpha_{jk} \mathbf{u}(\mathbf{x}_{j-1}) \Delta t \quad (j = 1, 2, 3), \quad (4)$$

where $\mathbf{x}_0 = \mathbf{x}(t)$ and $\mathbf{x}(t+\Delta t) = \mathbf{x}_3$, and α_{jk} are the empirical parameters (see Drummond et al. (1984) for the values).

The velocity within the cells is calculated using trilinear interpolation. Suppose the particle location (x, y, z) is within a voxel cornered by eight lattice points (x_0, y_0, z_0) , (x_0, y_0, z_1) , (x_0, y_1, z_1) , (x_0, y_1, z_0) , (x_1, y_0, z_0) , (x_1, y_0, z_1) , (x_1, y_1, z_1) and (x_1, y_1, z_0) , where $x_1 - x_0 = \Delta x$, $y_1 - y_0 = \Delta y$, and $z_1 - z_0 = \Delta z$. We write the flow velocity at each lattice point by \mathbf{u}_{000} , \mathbf{u}_{001} , \mathbf{u}_{011} , \mathbf{u}_{010} , \mathbf{u}_{100} , \mathbf{u}_{101} , \mathbf{u}_{111} and \mathbf{u}_{110} , respectively. The flow velocity at the point (x, y, z) is written as

$$\mathbf{u}(x, y, z) = \mathbf{u}_{000}(1-x_d)(1-y_d)(1-z_d) + \mathbf{u}_{100}x_d(1-y_d)(1-z_d) \quad (5)$$

$$+ \mathbf{u}_{010}(1-x_d)y_d(1-z_d) + \mathbf{u}_{110}x_dy_d(1-z_d) \quad (6)$$

$$+ \mathbf{u}_{001}(1-x_d)(1-y_d)z_d + \mathbf{u}_{101}x_d(1-y_d)z_d \quad (7)$$

$$+ \mathbf{u}_{011}(1-x_d)y_dz_d + \mathbf{u}_{111}x_dy_dz_d, \quad (8)$$

where

$$x_d = \frac{x - x_0}{\Delta x} \quad (9)$$

$$y_d = \frac{y - y_0}{\Delta y} \quad (10)$$

$$z_d = \frac{z - z_0}{\Delta z}. \quad (11)$$

To mitigate numerical errors, we implemented an adaptive time-step control using the step-doubling scheme (Press et al., 1992). The initial time step interval is set to (de Dreuzy et al., 2007; Tajima, Dentz, et al., 2024)

$$\Delta t^0 = 0.1 \max \left[\frac{\Delta x}{\max(u_x)}, \frac{\Delta y}{\max(u_y)}, \frac{\Delta z}{\max(u_z)} \right]. \quad (12)$$

After calculating the particle location at a time step t^n with Equation (4), the next time-step interval $\Delta t^{n+1} = t^{n+2} - t^{n+1}$ is determined by the following procedure (Diersch, 2013; Tajima, Dentz, et al., 2024):

1. Calculate the particle location \mathbf{x}_m^{n+1} for a full time step Δt with Equation (4).
2. Calculate the location of the particles $\widetilde{\mathbf{x}}_m^{n+1/2}$ for a half-step $\Delta t/2$ with Equation (4). Then, $\widetilde{\mathbf{x}}_m^{n+1}$ (the location of the particles after the two half steps) is calculated similarly for the remaining half step $\Delta t/2$ with $\mathbf{x}_m^{n+1/2}$.
3. Calculate the maximum relative difference d^{n+1} between \mathbf{x}_m^{n+1} and $\widetilde{\mathbf{x}}_m^{n+1}$ by

$$d^{n+1} = \max \left(\frac{|x_m^{n+1} - \widetilde{x}_m^{n+1}|}{|x^n| + |u_x^n \Delta t|}, \frac{|y_m^{n+1} - \widetilde{y}_m^{n+1}|}{|y^n| + |u_y^n \Delta t|}, \frac{|z_m^{n+1} - \widetilde{z}_m^{n+1}|}{|z^n| + |u_z^n \Delta t|} \right). \quad (13)$$

4. Determine Δt^{n+1} by

$$\Delta t^{n+1} = \begin{cases} 0.9 \Delta t^n \left(\frac{\varepsilon}{d^{n+1}} \right)^{\frac{1}{4}} & \text{if } d^{n+1} \leq \varepsilon \\ 0.9 \Delta t^n \left(\frac{\varepsilon}{d^{n+1}} \right)^{\frac{1}{3}} & \text{if } d^{n+1} > \varepsilon \end{cases}, \quad (14)$$

where ε ($= 10^{-3}$ in this study) is the pre-defined maximum error.

Appendix C. Parameters for numerical simulations

Table 1 summarises the parameters used in the numerical simulations, including the density-dependent flow and transport simulations with MODFLOW 6 (Langevin et al., 2017) and the particle tracking simulations for purely advective contaminant transport.

Table 1. Parameters for numerical simulations

| Parameter | Value | Unit |
|---|---------------------------|----------------------------|
| Domain size ($L_x \times L_y \times L_z$) | $100 \times 50 \times 10$ | m |
| Geometric mean hydraulic conductivity (K_G) | 3.5 | m d^{-1} |
| Log-conductivity variance (σ_f^2) | 0.5, 1, 2, 4 | – |
| Correlation lengths ($\lambda_x \times \lambda_y \times \lambda_z$) | $5 \times 5 \times 2$ | m |
| Grid sizes ($\Delta_x \times \Delta_y \times \Delta_z$) | $1 \times 1 \times 0.25$ | m |
| Amplitude (A) | 0.5 | m |
| Period (τ) | 0.5 | d |
| Specific storage (S_s) | 1×10^{-2} | m^{-1} |
| Porosity | 0.25 | – |
| Terrestrial flux (q_f) | 1×10^{-3} | m d^{-1} |
| Longitudinal dispersivity | 0.5 | m |
| Transverse dispersivity | 0.05 | m |
| Molecular diffusivity ¹ | 8.64×10^{-5} | $\text{m}^2 \text{d}^{-1}$ |
| Freshwater density | 1.0000×10^{-3} | kg m^{-3} |
| Seawater density | 1.0245×10^{-3} | kg m^{-3} |
| Gravitational acceleration | 9.8 | m s^{-2} |
| Viscosity | 1.124×10^{-3} | Pa s |

For calculating and illustrating travel distances, breakthrough curves, and Poincaré sections, a total of 36,531 particles are seeded at 0.1 and 0.05 m intervals in y - and z -directions. For calculating the mixing entropy and segregation intensity at a total of 181,101 particles are seeded at 0.05 and 0.02 m intervals in each direction.

Acknowledgments

ST acknowledges insightful suggestions from Niels Hartog. MD acknowledges funding by the European Union (ERC, KARST, 101071836). Views and opinions expressed are, however, those of the authors only, and do not necessarily reflect those of the European Union or the European Research Council Executive Agency. Neither the European Union nor the granting authority can be held responsible for them. The authors declare no competing interests.

References

- Adolf, J. E., Burns, J., Walker, J. K., & Gamiao, S. (2019). Near shore distributions of phytoplankton and bacteria in relation to submarine groundwater discharge-fed fishponds, kona coast, hawai ‘i, usa. *Estuarine, Coastal and Shelf Science*, 219, 341–353.
- Bear, J. (1972). *Dynamics of fluids in porous media*. American Elsevier, New York.
- Blanco, A. C., Watanabe, A., Nadaoka, K., Motooka, S., Herrera, E. C., & Yamamoto, T. (2011). Estimation of nearshore groundwater discharge and its potential effects on a fringing coral reef. *Marine pollution bulletin*, 62(4), 770–785.
- Camesasca, M., Kaufman, M., & Manas-Zloczower, I. (2006). Quantifying fluid mixing with the shannon entropy. *Macromolecular theory and simulations*, 15(8),

¹ Only applied to the density-dependent flow and transport simulations with MODFLOW. In the particle tracking simulations for a contaminant, molecular diffusivity is zero (purely advective).

595–607.

- Cho, H.-M., Kim, G., & Shin, K.-H. (2019). Tracing nitrogen sources fueling coastal green tides off a volcanic island using radon and nitrogen isotopic tracers. *Science of the Total Environment*, *665*, 913–919.
- Danckwerts, P. (1952). The definition and measurement of some characteristics of mixtures. *Applied Scientific Research, Section A*, *3*, 279–296.
- de Dreuzy, J.-R., Beaudoin, A., & Erhel, J. (2007). Asymptotic dispersion in 2d heterogeneous porous media determined by parallel numerical simulations. *Water Resources Research*, *43*(10).
- De Vriendt, K., Pool, M., & Dentz, M. (2020). Heterogeneity-induced mixing and reaction hot spots facilitate karst propagation in coastal aquifers. *Geophysical Research Letters*, *47*(10), e2020GL087529.
- Diersch, H.-J. G. (2013). *Feflow: finite element modeling of flow, mass and heat transport in porous and fractured media*. Springer Science & Business Media.
- Drummond, I., Duane, S., & Horgan, R. (1984). Scalar diffusion in simulated helical turbulence with molecular diffusivity. *Journal of Fluid Mechanics*, *138*, 75–91.
- Geng, X., Boufadel, M. C., Rajaram, H., Cui, F., Lee, K., & An, C. (2020). Numerical study of solute transport in heterogeneous beach aquifers subjected to tides. *Water Resources Research*, *56*(3), e2019WR026430.
- Geng, X., Michael, H. A., Boufadel, M. C., Molz, F. J., Gerges, F., & Lee, K. (2020). Heterogeneity affects intertidal flow topology in coastal beach aquifers. *Geophysical Research Letters*, *47*(17), e2020GL089612.
- Guo, W., & Langevin, C. D. (2002). *User's guide to seawat: a computer program for simulation of three-dimensional variable-density ground-water flow* (Vol. 1) (No. 434). US Geological Survey.
- Heiss, J. W., Post, V. E., Laattoe, T., Russoniello, C. J., & Michael, H. A. (2017). Physical controls on biogeochemical processes in intertidal zones of beach aquifers. *Water Resources Research*, *53*(11), 9225–9244.
- Hwang, D.-W., Lee, Y.-W., & Kim, G. (2005). Large submarine groundwater discharge and benthic eutrophication in bangdu bay on volcanic jeju island, korea. *Limnology and Oceanography*, *50*(5), 1393–1403.
- Inouchi, K., Kishi, Y., & Kakinuma, T. (1990). The motion of coastal groundwater in response to the tide. *Journal of Hydrology*, *115*(1), 165–191. doi: [https://doi.org/10.1016/0022-1694\(90\)90203-A](https://doi.org/10.1016/0022-1694(90)90203-A)
- Kubo, R., Toda, M., & Hashitsume, N. (2012). *Statistical physics ii: nonequilibrium statistical mechanics* (Vol. 31). Springer Science & Business Media.
- Kwon, H. K., Kang, H., Oh, Y. H., Park, S. R., & Kim, G. (2017). Green tide development associated with submarine groundwater discharge in a coastal harbor, jeju, korea. *Scientific reports*, *7*(1), 6325.
- Langevin, C. D., Hughes, J. D., Banta, E. R., Niswonger, R. G., Panday, S., & Provost, A. M. (2017). *Documentation for the modflow 6 groundwater flow model* (Tech. Rep.). US Geological Survey.
- Langevin, C. D., Panday, S., & Provost, A. M. (2020). Hydraulic-head formulation for density-dependent flow and transport. *Groundwater*, *58*(3), 349–362.
- Lee, Y.-W., Hwang, D.-W., Kim, G., Lee, W.-C., & Oh, H.-T. (2009). Nutrient inputs from submarine groundwater discharge (sgd) in masan bay, an embayment surrounded by heavily industrialized cities, korea. *Science of the total environment*, *407*(9), 3181–3188.
- Liu, Y., Jiao, J. J., & Liang, W. (2018). Tidal fluctuation influenced physicochemical parameter dynamics in coastal groundwater mixing zone. *Estuaries and Coasts*, *41*, 988–1001.
- Michael, H. A., Scott, K. C., Koneshloo, M., Yu, X., Khan, M. R., & Li, K. (2016). Geologic influence on groundwater salinity drives large seawater circulation through the continental shelf. *Geophysical Research Letters*, *43*(20), 10–782.
- Moore, W. S. (1999a). The subterranean estuary: A reaction zone of ground wa-

- ter and sea water. *Marine Chemistry*, 65(1-2), 111–125. doi: 10.1016/S0304-4203(99)00014-6
- Moore, W. S. (1999b). The subterranean estuary: a reaction zone of ground water and sea water. *Marine chemistry*, 65(1-2), 111–125.
- Mulligan, A. E., Langevin, C., & Post, V. E. (2011). Tidal boundary conditions in seawater. *Groundwater*, 49(6), 866–879.
- Oberdorfer, J. A., Hogan, P. J., & Buddemeier, R. W. (1990). Atoll island hydrogeology: flow and freshwater occurrence in a tidally dominated system. *Journal of Hydrology*, 120(1-4), 327–340.
- Pool, M., & Dentz, M. (2018). Effects of heterogeneity, connectivity, and density variations on mixing and chemical reactions under temporally fluctuating flow conditions and the formation of reaction patterns. *Water Resources Research*, 54(1), 186–204.
- Pool, M., Post, V. E., & Simmons, C. T. (2014). Effects of tidal fluctuations on mixing and spreading in coastal aquifers: Homogeneous case. *Water Resources Research*, 50(8), 6910–6926.
- Pool, M., Post, V. E., & Simmons, C. T. (2015). Effects of tidal fluctuations and spatial heterogeneity on mixing and spreading in spatially heterogeneous coastal aquifers. *Water Resources Research*, 51(3), 1570–1585.
- Press, W. H., Teukolsky, S. A., Vetterling, W. T., & Flannery, B. P. (1992). *Numerical recipes in C* (Second ed.). Cambridge, USA: Cambridge University Press.
- Renard, P., & De Marsily, G. (1997). Calculating equivalent permeability: a review. *Advances in water resources*, 20(5-6), 253–278.
- Rezaei, M., Sanz, E., Raeisi, E., & Ayora, C. (2005). Reactive transport modeling of calcite dissolution in the fresh-salt water mixing zone. *Journal of Hydrology*, 311, 282–298. doi: 10.1016/j.jhydrol.2004.12.017
- Robinson, C., Brovelli, A., Barry, D., & Li, L. (2009). Tidal influence on btx biodegradation in sandy coastal aquifers. *Advances in Water Resources*, 32(1), 16–28.
- Robinson, C., Gibbes, B., & Li, L. (2006). Driving mechanisms for groundwater flow and salt transport in a subterranean estuary. *Geophysical Research Letters*, 33(3).
- Robinson, C. E., Xin, P., Santos, I. R., Charette, M. A., Li, L., & Barry, D. A. (2018). Groundwater dynamics in subterranean estuaries of coastal unconfined aquifers: Controls on submarine groundwater discharge and chemical inputs to the ocean. *Advances in Water Resources*, 115, 315–331.
- Rubin, Y. (2003). *Applied stochastic hydrogeology*. New York: Oxford University Press.
- Sanford, W. E., & Konikow, L. F. (1989). Simulation of Calcite Dissolution and Porosity Changes in Saltwater Mixing Zones in Coastal Aquifers. *Water Resources Research*, 25(4), 655–667.
- Santos, I. R., Chen, X., Lecher, A. L., Sawyer, A. H., Moosdorf, N., Rodellas, V., . . . others (2021). Submarine groundwater discharge impacts on coastal nutrient biogeochemistry. *Nature Reviews Earth & Environment*, 2(5), 307–323.
- Schrama, E., & Ray, R. (1994). A preliminary tidal analysis of topex/poseidon altimetry. *Journal of Geophysical Research: Oceans*, 99(C12), 24799–24808.
- Schwiderski, E. W. (1980). On charting global ocean tides. *Reviews of geophysics*, 18(1), 243–268.
- Spiteri, C., Slomp, C. P., Tuncay, K., & Meile, C. (2008). Modeling biogeochemical processes in subterranean estuaries : Effect of flow dynamics and redox conditions on submarine groundwater discharge of nutrients. *Water Resources Research*, 44, 1–18. doi: 10.1029/2007WR006071
- Strogatz, S. H. (2001). *Nonlinear dynamics and chaos*. Perseus Books, Reading, Massachusetts.
- Tajima, S., Brunner, P., Liu, J., Delottier, H., & Tokunaga, T. (2023). Ground-

- water flooding on atolls caused by storm surges: Effects of the dual-aquifer configuration. *Water Resources Research*, 59(10), e2023WR034762.
- Tajima, S., & Dentz, M. (2024). Dispersion and mixing in heterogeneous compressible porous media under transient forcing. *arXiv preprint arXiv:2409.16789*.
- Tajima, S., Dentz, M., Liu, J., & Tokunaga, T. (2024). Time-dependent dispersion coefficients for the evolution of displacement fronts in heterogeneous porous media. *Advances in Water Resources*, 104714. doi: 10.1016/j.advwatres.2024.104714
- Tajima, S., Liu, J., & Tokunaga, T. (2022). Estimating freshwater lens volume in highly permeable aquifers. *Hydrological Research Letters*, 16(1), 12–17.
- Tajima, S., Liu, J., & Tokunaga, T. (2024). Mechanisms of non-fresh groundwater presence at water tables in highly permeable coastal aquifers. *Groundwater*, 62(4), 527–536.
- Taniguchi, M., Dulai, H., Burnett, K. M., Santos, I. R., Sugimoto, R., Stieglitz, T., ... Burnett, W. C. (2019). Submarine groundwater discharge: updates on its measurement techniques, geophysical drivers, magnitudes, and effects. *Frontiers in Environmental science*, 7, 141.
- Trefry, M., Lester, D., Metcalfe, G., & Wu, J. (2019). Temporal fluctuations and poroelasticity can generate chaotic advection in natural groundwater systems. *Water Resources Research*, 55(4), 3347–3374.
- Trefry, M., Lester, D., Metcalfe, G., & Wu, J. (2020). Lagrangian complexity persists with multimodal flow forcing in compressible porous systems. *Transport in Porous Media*, 135(3), 555–586.
- Waska, H., & Kim, G. (2010). Differences in microphytobenthos and macrofaunal abundances associated with groundwater discharge in the intertidal zone. *Marine Ecology Progress Series*, 407, 159–172.
- Waska, H., & Kim, G. (2011). Submarine groundwater discharge (sgd) as a main nutrient source for benthic and water-column primary production in a large intertidal environment of the yellow sea. *Journal of Sea Research*, 65(1), 103–113.
- Werner, A. D., Bakker, M., Post, V. E., Vandenbohede, A., Lu, C., Ataie-Ashtiani, B., ... Barry, D. A. (2013). Seawater intrusion processes, investigation and management: Recent advances and future challenges. *Advances in water resources*, 51, 3–26.
- Wu, J., Lester, D., Trefry, M. G., & Metcalfe, G. (2024). Lagrangian coherent structures control solute dispersion in heterogeneous poroelastic media. *Physical Review Fluids*, 9(4), 044501.
- Wu, J., Lester, D. R., Trefry, M. G., & Metcalfe, G. (2020). When do complex transport dynamics arise in natural groundwater systems? *Water Resources Research*, 56(2), e2019WR025982.